Geosci. Model Dev. Discuss., 5, 2999–3033, 2012
www.geosci-model-dev-discuss.net/5/2999/2012/
doi:10.5194/gmdd-5-2999-2012

Geoscientific Model Development Discussions

MESMO 2: a mechanistic marine silica cycle and coupling to a simple terrestrial scheme

K. Matsumoto[1], K. S. Tokos[1], A. Huston[2], and H. Joy-Warren[3]

[1]Department of Earth Sciences, University of Minnesota, Minneapolis, Minnesota, USA
[2]University of California, Santa Cruz, California, USA
[3]University of Chicago, Chicago, Illinois, USA

Received: 20 June 2012 – Accepted: 17 September 2012 – Published: 24 September 2012

Correspondence to: K. Matsumoto (katsumi@umn.edu)

Published by Copernicus Publications on behalf of the European Geosciences Union.

Abstract

Here we describe the second version of Minnesota Earth System Model for Ocean biogeochemistry (MESMO 2), an earth system model of intermediate complexity, which consists of a dynamical ocean, dynamic-thermodynamic sea ice, and energy moisture balanced atmosphere. The new version has more realistic land ice masks and is driven by seasonal winds. A major aim in version 2 is representing the marine silica cycle mechanistically in order to investigate climate-carbon feedbacks involving diatoms, a critically important class of phytoplankton in terms of carbon export production. This is achieved in part by including iron, on which phytoplankton uptake of silicic acid depends. Also, MESMO 2 is coupled to an existing terrestrial model, which allows for the exchange of carbon, water, and energy between land and the atmosphere. The coupled model, called MESMO 2E, is appropriate for more complete earth system simulations. The new version was calibrated with the goal of preserving reasonable interior ocean ventilation and various biological production rates in the ocean and land, while simulating key features of the marine silica cycle.

1 Introduction

Here we document development of the second version of the Minnesota Earth System Model for Ocean biogeochemistry (MESMO 2). The first version described earlier (Matsumoto et al., 2008) is based on a non-modular version of the Grid ENabled Integrated Earth system model (GENIE; http://www.genie.ac.uk/), which in turn is based on the computationally efficient ocean-climate model of Edwards and Marsh (2005). This work is independent of the efforts of the GENIEfy project to develop different flavors of the modularized GENIE.

MESMO has a 3-D dynamical ocean, 2-D energy-moisture balanced atmosphere, dynamic and thermodynamic sea ice, and prognostic marine biogeochemistry. It is an earth system model of intermediate complexity (EMIC), a group which occupies an important and unique position within the hierarchy of climate models (Claussen et al., 2002). EMICs represent a compromise between high resolution, comprehensive coupled models of atmospheric and oceanic circulation, which require significant computational resources, and conceptual (box) models, which are computationally very efficient but represent the climate system in a highly idealized manner. As an EMIC, MESMO retains important dynamics, which allow for simulations of transient climate change, while remaining computationally efficient. The efficiency is achieved by reducing spatial resolution as well as the number and detail of processes compared to high resolution coupled models.

Calibration of the earlier MESMO 1 benefited from multi-objective tuning of the physical model parameters, whereby the mismatch between model-simulated fields and equivalent observed fields was minimized. The equilibrium run of MESMO 1 is well calibrated with respect to oceanic uptake of anthropogenic transient tracers, chlorofluorocarbons, anthropogenic carbon, and radiocarbon (Matsumoto et al., 2008). These tracers reflect ocean ventilation over decades to a century by intermediate waters in the upper ocean as well as by the relatively rapid North Atlantic Deep Water. The model is also well calibrated on centennial time scales with respect to the abundance of natural ^{14}C ($\Delta^{14}C$) in the deep Pacific and Indian Oceans. MESMO 1 has been used successfully in a number of carbon and climate process studies (Lee et al., 2011; Matsumoto et al., 2010; Sun and Matsumoto, 2010; Ushie and Matsumoto, 2012) as well as in model intercomparison projects (Archer et al., 2009; Cao et al., 2009; Eby et al., 2012; Joos et al., 2012; Weaver et al., 2012; Zickfeld et al., 2012).

A strong motivation for developing MESMO 2 was to investigate the climate-carbon feedbacks involving diatoms, which were not represented in MESMO 1. Diatoms are critical in the ocean carbon cycle, because they are by far the most important agent of vertical transport of carbon from the surface to the deep ocean (Armstrong et al., 2002). Diatoms can account for most of the carbon export production that takes place in the Southern Ocean and more than 50 % globally (Sarmiento and Gruber, 2006). Diatom production is often limited by the availability of silicic acid ($Si(OH)_4$). A mechanistic

GMDD
5, 2999–3033, 2012

representation of the marine silica cycle in the model requires iron (Fe), because the uptake of $Si(OH)_4$ by diatoms depends of the bioavailability of Fe. MESMO 2 therefore has $Si(OH)_4$ and Fe as new tracers.

Another motivation for this work is to have a model that includes a terrestrial scheme, so that the global carbon cycle encompassing the atmosphere, ocean, and land can be simulated. A terrestrial scheme with prognostic land surface albedo would also allow land albedo feedback in global climate change simulations. In this regard, we make use of the existing model ENTS (efficient numerical terrestrial scheme), coupled previously to GENIE (Williamson et al., 2006). MESMO 2 coupled to ENTS is here referred to as MESMO 2E. In this work, the equilibrium simulations of MESMO 2 and MESMO 2E are described. Key diagnostics of their equilibrium states are summarized in Table 1.

2 New features of MESMO 2

In the following two sections, we describe the main new physical and biogeochemical modifications and additions which were adopted in MESMO 2 (Table 2).

2.1 New physical features

In MESMO 1, surface albedo is only a function of latitude and ranges from 0.2 at low latitudes to 0.5 at high latitudes. In contrast, sea ice albedo depends on temperature and yields more realistic values reaching as high as 0.7. These disparate calculations in MESMO 1 produce a rather unrealistic situation whereby both Greenland and Antarctic ice sheets have surface albedo values that are too low, even lower than sea ice located at lower latitudes.

In MESMO 2, we correct this situation by specifying land masks for Greenland and Antarctica with higher albedo (Table 2). Since this increases the surface albedo globally, it is necessary to compensate for this by reducing the planetary albedo by 3.5 %,

GMDD
5, 2999–3033, 2012

to bring the annual mean surface air temperature reasonably close to the observed value (Table 1).

The second important change made in MESMO 2 is the replacement of the annual mean wind stress field used in MESMO 1 with seasonal wind stress fields to drive ocean dynamics (Table 2). Following GENIE's core climate model (Edwards and Marsh, 2005), MESMO 1 uses the annual mean wind stress data from Southampton Oceanography Centre (SOC) climatology (Josey et al., 1998). This is replaced in MESMO 2 with the monthly mean wind stress fields from the European Centre for Medium-Range Weather Forecasts (ECMWF) reanalysis for the period 1980–1989 (Trenberth et al., 1989) As noted by Josey et al. (2002), the reanalysis winds are approximately 40 % stronger over the Southern Ocean than observation-based winds such as the SOC winds. As a result, the introduction of the seasonal ECMWF wind stress fields in MESMO 2 greatly strengthens its ocean ventilation, so that the deep ocean $\Delta^{14}C$ becomes unrealistically young. In MESMO 1, $\Delta^{14}C$ of the North Atlantic Deep Water (NADW), Circumpolar Deep Water (CDW), and North Pacific Deep Water (NPDW) is respectively −99 ‰, −153 ‰, and −216 ‰. These values are in good agreement with observed, natural $\Delta^{14}C$ values (Table 1). The use of the ECMWF winds alone increases them to −80 ‰, −104 ‰, and −129 ‰, respectively.

In order to correct this excessive ventilation, we removed the artificial wind stress scaling factor everywhere except in the far North Atlantic. A scaling factor of about 2 was introduced originally by Edwards and Marsh (2005) to realize sufficiently strong wind driven circulation, and that factor is carried forward in MESMO 1. If the scaling is removed completely while using the seasonal ECMWF winds, the excessive deep ventilation is significantly reduced and the deep $\Delta^{14}C$ distribution improves; however, the Atlantic meridional overturning circulation (MOC) becomes too weak (6 Sv; $Sv = 10^6\,m^3\,s^{-1}$). Therefore, in order to maintain the Atlantic MOC to a reasonable strength in MESMO 2, the wind scaling of 2 is kept just in the North Atlantic. Also, the Atlantic-to-Pacific freshwater flux adjustment was increased from 0.2 to 0.3 Sv in the northern hemisphere, but reduced in the southern hemisphere by the same amount, so

GMDD
5, 2999–3033, 2012

that the basis-wide adjustment remains unchanged. With these changes, the Atlantic MOC is 12 Sv in MESMO 2 and 17 Sv in MESMO 2E (Table 1).

In MESMO 1, the winds that drove the different components of the model were different wind products. For example, the wind stress fields that drove ocean dynamics were not consistent with the wind speed fields that drove air-sea gas exchange. And winds that drove evaporation, precipitation, and the transport of heat and moisture in the 2-D atmospheric model were different still. In version 2, all components of the model, including the terrestrial model ENTS are now consistently driven by the same seasonal ECMWF winds.

2.2 New biogeochemical features

The limiting nutrients in MESMO 1 are phosphate (PO_4), nitrate (NO_3), and aqueous CO_2, whose uptake is governed by Michaelis-Menton kinetics with calibrated half saturation rates. Organic carbon production is assumed to be carried out by only one generic class of phytoplankton. In MESMO 2, Fe and $Si(OH)_4$ are added as limiting nutrients, and phytoplankton is represented by two size classes, large and small.

The nutrient dependence of growth for the small phytoplankton (SP) is limited by the total Fe (FeT), PO_4, NO_3, and CO_2:

$$F_N = \min\left\{\frac{FeT}{FeT + K_{FeT}}\cdot FeT, \frac{PO_4}{PO_4 + K_{PO_4}}\cdot PO_4, \frac{NO_3}{NO_3 + K_{NO_3}}\cdot NO_3, \frac{CO_2}{CO_2 + K_{CO_2}}\cdot CO_2\right\}$$

where K_X's are half-saturation concentrations in the usual Michaelis-Menton formulation of nutrient uptake kinetics (Table 2). The most limiting nutrient is identified and its uptake rate determined by the minimum of the above equation. The uptake for other nutrients are related to the limiting nutreint by the particulate organic matter (POM) elemental stoichiometry: P:N:C=1:16:117 and the ratio involving Fe is variable as noted below. SP growth is also dependent on light, mixed layer depth, temperature, and biomass; these dependences remain the same as in MESMO 1. $CaCO_3$-forming phytoplankton such as coccolithophorids is assumed to be part of SP in MESMO 2. The

GMDD
5, 2999–3033, 2012

dependence of $CaCO_3$ production on carbonate ion saturation concentration remains the same as in MESMO 1.

The large phytoplankton class (LP) essentially represents diatoms, so its nutrient dependence term is further limited by silicic acid with an additional term for $Si(OH)_4$ in the above equation. The stoichiometry relating particulate organic carbon (POC) to Si is set to 1.0. The growth of LP depends also on light, mixed layer depth, temperature, and biomass. For all nutrients, smaller values of Kx are assigned to SP, so they have a competitive advantage in low nutrient environments over LP. This accounts for the larger surface area to volume ratio that facilitates a faster diffusive uptake of nutrients by SP.

Since diatoms are commonly assumed to be competitive when $Si(OH)_4$ is available, LP increases until $Si(OH)_4$ is nearly completely drawn down. The rate of $Si(OH)_4$ utilization follows the Michaelis-Menton kinetics with a half saturation concentration shown in Table 2. Silicic acid utilization also depends on the bioavailability of iron such that its uptake relative to nitrate (i.e., the Si:N uptake ratio) increases with decreasing iron (Franck et al., 2000; Hutchins and Bruland, 1998; Takeda, 1998). In MESMO 2, Si:N uptake follows an inverse relation ($\text{Si:N}=0.2\times10^{-9}\cdot[\text{Fe}]^{-1}$, where [Fe] is mol-Fe kg^{-1}), with minimum value capped at 0.3 following the data-based estimation (Sarmiento et al., 2004).

Within the water column, opal particles experience dissolution, whose rate depends on the ambient temperature and whether the local seawater is under- or over-saturated with respect to the solid phase. The formulation for water column dissolution, including parameter values, follows Ridgwell et al. (2002). Because MESMO 2 is not coupled to a sediment model, any particle that reaches the sea floor dissolves completely and $Si(OH)_4$ is returned to the overlying water.

MESMO 2 calculates δ^{30}Si in seawater or the relative abundance of ^{30}Si compared to the more common and lighter isotope ^{28}Si. Because marine diatoms fractionate against ^{30}Si during silicic acid fixation, δ^{30}Si is believed to reflect the degree to which $Si(OH)_4$ is utilized by diatoms (De La Rocha et al., 1998). The fractionation factor during $Si(OH)_4$ fixation in MESMO 2 is set to 0.9989 or −1.1 ‰ (De La Rocha et al., 1997).

MESMO 2 includes the basic Fe code as it existed within the GENIE framework as of May, 2009. The code follows the seminal modeling work of Archer and Johnson (2000), who gave a prominent role for organic iron-binding ligands in controlling the oceanic FeT concentration. While the vertical profile of FeT is nutrient-like (depleted at surface), the deep ocean distribution of FeT does not exhibit the classic Atlantic-to-Pacific increase in nutrients. Although recent work indicates slightly lower FeT in the Pacific versus the Atlantic (Boyd and Ellwood, 2010), the deep ocean concentration has long been considered relatively homogeneous. As assumed by Archer and Johnson (2000), the observed FeT distribution is typically explained and modeled in terms of both iron complexation to organic ligands and removal by scavenging (Johnson et al., 1997).

In MESMO 2, iron is introduced into the ocean as soluble portion of atmospheric dust (3.5 % of dust is assumed to be iron with fractional solubility of 0.2 %). The dust flux field is taken from Mahowald (2003). Most of the dust-derived, soluble Fe is quickly bound to organic ligands according to the conditional stability scheme of Parekh et al. (2005) or scavenged by the sinking POM. FeT is thus the sum of free dissolved Fe, which occurs in very small concentrations, and the more abundant ligand-bound Fe (FeL). In the model, phytoplankton can uptake either free Fe or FeL, and the uptake occurs with a variable C:Fe ratio, which is apparently dependent on FeT (Sunda and Huntsman, 1995). Phytoplankton uses iron more efficiently in low FeT waters, so that the uptake C:Fe ratio can reach as high as 200,000 in the model. As POM sinks, iron is remineralized along with other nutrients and can subsequently become scavenged again by POM or become ligand-bound and exist in the water column. The scavenged iron which escapes remineralization and reaches the sea floor is then assumed to be buried in the sediments and removed from the model domain. This removal over time will balance the aeolian input at the surface.

The two important parameters of the iron code are the scavenging rate, which determines how quickly iron is removed from the water column, and the ligand binding strength, which is related to the conditional stability scheme (Table 1). As the binding

GMDD
5, 2999–3033, 2012

strength becomes greater, iron will become more strongly bound to ligands, increasing FeL and thus FeT in the water column. The concentration of ligand is set at 1 nm.

Finally, as noted previously (Matsumoto et al., 2010), there was a minor error in the code of MESMO 1 with respect to $CaCO_3$ remineralization. It has an exponential formulation with a Q_{10}=2 dependence on temperature; the dependence is similar to POC remineralization but weaker for $CaCO_3$. The erroneous formation dissolves more $CaCO_3$ than exists under some conditions, so the fix introduces a cap on the maximum dissolution to prevent such unrealistic situation. MESMO 2 includes this fix, which changes the global $CaCO_3$ production by less than 1 %. Also, in contrast to MESMO 1, global ocean CO_2 chemistry is now recalculated immediately prior to model output, so that all outputs reflect the model state at the same time.

3 Terrestrial scheme ENTS and MESMO 2E

MESMO 2E couples MESMO 2 to the terrestrial scheme, ENTS (Williamson et al., 2006), which exists as an optional module within the GENIE framework. It is a simple prognostic model of land biosphere that calculates the exchange of energy, moisture, and carbon between land and the atmosphere. Global fluxes of carbon from photosynthesis, plant and soil respiration, and leaf litter drive carbon stocks of land vegetation and soil. Photosynthesis has dependence on atmospheric CO_2, water stress, air temperature, and biomass or vegetation fraction. Land vegetation is expressed as fractional coverage with corresponding albedo based on vegetation, soil cover, and soil type. Prognostic variables include vegetation and soil carbon as well as land surface albedo and temperature. Also, as noted above, the seasonal NCEP reanalysis winds, which drove ENTS in Williamson et al. (2006), are replaced in MESMO 2E by the same seasonal ECMWF reanalysis winds that drive the ocean and atmosphere. The two reanalysis products are actually quite similar, so the replacement has little impact on overall model performance, but it elevates the level of consistency in the new model boundary conditions.

GMDD
5, 2999–3033, 2012

The original ENTS did not have carbon isotopes, which were added in MESMO 2E. During phytosynthesis, land plants preferentially fix the lighter ^{12}C over ^{13}C and ^{14}C, so that the biosphere becomes isotopically light and ambient air becomes heavy. In the model, a photosynthetic fractionation factor is set to 0.9815 (i.e., −18.5‰) for ^{13}C and twice as large for ^{14}C. No fractionation is assumed for other terrestrial carbon processes.

Following Williamson et al. (2006), MESMO 2E is calibrated by adjusting a set of rate parameters in ENTS that relate to photosynthesis, vegetation respiration, litter, and soil respiration. In this work, three parameters, namely k18, k24, and k29, are adjusted to match preindustrial global vegetation stock (Olson et al., 1983), soil carbon stock (Batjes, 1995), and global carbon fluxes from IPCC (Houghton et al., 2001) (Tables 1, 2). The adjustments represent reductions of 45 % in k18, 20 % in k24, and 48 % in k29 relative to the values chosen by Williamson et al. (2006).

The adjustments made in ENTS caused changes in the land surface properties such that the land surface albedo increased and global temperatures became lower by more than 1 °C. In order to compensate for this cooling, planetary albedo in MESMO 2E is reduced from MESMO 2, so that the total change relative to MESMO 1 is increased to −5.5 % (Table 2).

4 Equilibrium Runs of MESMO 2 and 2E

Since MESMO is a tool developed primarily to investigate ocean biogeochemistry, these models were calibrated with the goal of having reasonable ocean physics with greater attention paid to reproducing key aspects of the marine silica cycle and ocean biogeochemistry in general.

With the ECMWF winds driving the ocean but with most of the wind scaling removed, MESMO 2 has about the same strength of the Atlantic MOC as MESMO 1 at 12 Sv (Fig. 1). It is stronger and more realistic in MESMO 2E at 17 Sv, which would tend to make the deep ocean younger in terms of $\Delta^{14}C$. Also, the spread in natural

$\Delta^{14}C$ between NADW and NPDW is not as large in the new models as in observations or MESMO 1 (Fig. 2). An important controlling factor of the spread is the degree to which air-sea gas exchange occurs when Antarctic Bottom Water (AABW) is formed in the models. In reality, various water mass transformation processes occur on the Antarctic continental shelves and under ice (e.g., Foster and Carmack, 1976) with very limited air-sea gas exchange. However, such localized processes are poorly represented in global models, in which open ocean convection with significantly more gas exchange typically plays an important role in AABW formation. The stronger reanalysis winds in the Southern Ocean (Josey et al., 2002) thus contribute to the smaller $\Delta^{14}C$ spread between NADW and NPDW in MESMO 2 and 2E (Fig. 2), but the spread is still about 100 ‰, which is comparable to the Ocean Carbon Cycle Intercomparison Project (OCMIP) models (Matsumoto et al., 2004). On decadal timescale, ocean ventilation is quite reasonable, as judged by the uptake of transient anthropogenic tracers CFC-11 and anthropogenic CO_2 (Table 1). The uptake for the year 1994 is 100 PgC of anthropogenic carbon for MESMO 2 and 101 PgC for MESMO 2E and 0.56×10^6 moles of CFC-11 for MESMO 2 and 0.59×10^6 moles for MESMO 2E. These are within the observational constraints of 118 ± 19 PgC(Sabine et al., 2004) and $0.55 \pm 0.12 \times 10^6$ moles CFC-11 (Willey et al., 2004) and compare well against OCMIP models (Matsumoto et al., 2004).

In MESMO 1, the global mean surface air temperature is about 2.5 °C colder than the observed annual mean of 14.0 °C (Jones et al., 1999). This is significantly improved in the new versions with the difference from observed now being 0.5 °C or less (Table 1). The coarse resolution of MESMO makes it difficult to sustain strong gradients of, for example, surface air temperature (Fig. 3) or sea surface temperature (Fig. 4). So, for air temperature, simulations tend to be longitudinally smooth; for sea surface temperature, the western warm pool is not as warm in the models.

In terms of seasonal sea ice extent, the new models show improvements over MESMO 1 but still overestimate it when compared to observation (Table 1, Fig. 5). Whereas MESMO 1 overestimates the sea ice extent in both hemispheres by 5–

GMDD
5, 2999–3033, 2012
MESMO 2: a mechanistic marine silica cycle
K. Matsumoto et al.

17×10^6 km, the overestimation in MESMO 2E is reduced to $2.5–5.5 \times 10^6$ km. The greater extent of sea ice in the far North Atlantic in all versions of MESMO compared to observation (Fig. 5) reflects the fact that open ocean convection that occurs in the Greenland-Ice Land-Norwegian Seas and leads to NADW formation occurs too far south in the models.

4.1 Ocean biogeochemistry

The values for the new biogeochemical parameters (Table 2) are tuned to simulate reasonable global production rates and spatial distributions of POC, $CaCO_3$, and opal (Table 1). At the same time, selected features of the iron and silica cycles were targeted. In terms of iron, targets include deep water FeT of 0.6–0.7 nmol kg^{-1} and Fe limitation in the Southern Ocean. The surface FeT must also be low enough for the Si:N uptake ratio to be elevated in the Southern Ocean and the far North Pacific (Sarmiento et al., 2004). Two other important targets with respect to the marine silica cycle are the export of $Si(OH)_4$-depleted waters from the Southern Ocean to the rest of the world ocean via Antarctic Intermediate and/or Mode Waters and the consequent $Si(OH)_4$ limitation for LP outside the Southern Ocean.

The global export production of POC is 11.9 PgC yr^{-1} in MESMO 2 and 12.5 PgC yr^{-1} in MESMO 2E (Table 1). These are consistent with a recent synthesis of particle export production, in which Dunne et al. (2007) give their best estimate as 9.6±3.6 PgC yr^{-1} for POC. Previous estimates ranged between 5.8 and 12.9 PgC yr^{-1}. Of the simulated global production, the majority is due to LP: 8.7 out of 11.9 PgC yr^{-1} in MESMO 2 and 9.2 out of 12.5 PgC yr^{-1} in MESMO 2E. As expected, total production is lowest in the nutrient poor oligotrophic gyres (Fig. 6a). The contribution of SP to the total production is highest in oligotrophic gyres, given the lower half saturation values in SP that give it competitive advantage over LP (Fig. 6b).

The simulated global $CaCO_3$ production is 1.0 PgC yr^{-1} by MESMO 2 and 0.9 PgC yr^{-1} by MESMO 2E (Table 1). These are comparable to MESMO 1 but higher

GMDD
5, 2999–3033, 2012

than the best estimate of Dunne et al. (2007) of $0.52 \pm 0.15\,\mathrm{PgC\,yr^{-1}}$. They note though that constraining the global $CaCO_3$ export has been controversial and that previous estimates ranged from 0.38 to $4.7\,\mathrm{PgC\,yr^{-1}}$ with most estimates occupying the lower end of the range.

The global export production of opal is also not well constrained by data. According to Dunne et al. (2007), historical estimates have ranged from 70 to $185\,\mathrm{Tmol\,Si\,yr^{-1}}$ (Tmol=10^{12} mol), while their best estimate is $101 \pm 35\,\mathrm{Tmol\,Si\,yr^{-1}}$. Global export is $130\,\mathrm{Tmol\,Si\,yr^{-1}}$ in MESMO 2 and $139\,\mathrm{Tmol\,Si\,yr^{-1}}$ in MESMO 2E (Table 1). The majority of the export production occurs in the Southern Ocean and a secondary peak in the North Pacific (Fig. 6c); the spatial pattern is consistent with Dunne et al. (2007).

In both MESMO 2 and 2E, FeT is higher in the Atlantic than in the Pacific. At depth, for example, FeT is approximately $0.65\,\mathrm{nmol\,kg^{-1}}$ in the Atlantic and about $0.6\,\mathrm{nmol\,kg^{-1}}$ in the Pacific. Available data also show lower FeT in the deep Pacific, which has the oldest waters and thus has experienced Fe scavenging the most (Boyd and Ellwood, 2010). At the surface, FeT is high in the North Atlantic, which reflects the large aeolian input of Fe from the African Sahara, and around Antarctica, where there is deep upwelling (Fig. 6d).

The subtropical gyres evident in terms of various diagnostics of model production (Fig. 6) clearly have depleted PO_4 concentrations in the top 100 m, although the depletion is stronger in observation (Fig. 7). Compared to MESMO 1, both MESMO 2 and 2E have a more pronounced and improved expression of eastern equatorial upwelling in terms of PO_4.

In the two new models, Fe is the limiting nutrient in the Southern Ocean for both SP and LP (Fig. 8). For SP, Fe is also limiting in the Arctic, but otherwise, nitrate is the limiting nutrient in much of the world ocean. For LP, or diatoms, $Si(OH)_4$ is the most limiting nutrient outside the Southern Ocean as observed (Sarmiento et al., 2004). There is no $Si(OH)_4$ limitation in the North Atlantic, where the high aeolian dust flux and thus high surface FeT lower both the Si:N uptake ratio and the demand for $Si(OH)_4$.

GMDD
5, 2999–3033, 2012

The North Pacific also does not experience $Si(OH)_4$ limitation, because the new models have elevated concentrations of $Si(OH)_4$ in the North Pacific (Fig. 9a) as generally observed. The silicic acid limitation in much of the low latitudes has its origin in the Southern Ocean, where Fe limitation causes Antarctic diatoms to utilize proportionally more $Si(OH)_4$ for a given amount of NO_3, so that Si:N utilization is generally elevated to ratios of 2.7 to 4.4 (Sarmiento et al., 2004). Also, as the same data analysis and our models show, the North Pacific is the other region where Si:N uptake is high (Fig. 9b). The models also capture the low Si:N uptake ratio in the North Atlantic as noted above. The high uptake rate of $Si(OH)_4$ in the Southern Ocean causes its depletion there. The degree to which $Si(OH)_4$ is depleted is commonly expressed in relation to nitrate as Si^* ($Si^*=[Si(OH)_4]-[NO_3]$). Negative values of Si^* indicate $Si(OH)_4$-depleted waters. With available data, it is possible to trace this Si^* signal originating from the Southern Ocean and spreading to the rest of the ocean via Antarctic Intermediate and Mode Waters (Brzezinski et al., 2002; Sarmiento et al., 2004). These are key features of the silica cycle that are simulated in both of our new models (Fig. 9c, d).

We note that these Si^* features provided the original motivation to develop MESMO 2. There is a hypothesis that the $Si(OH)_4$ depletion observed in the modern Southern Ocean can be reversed during times of high dust or iron input such as the glacial periods.. The consequent reorganization of the global silica cycle could help explain some of the variability in atmospheric CO_2 levels (Brzezinski et al., 2002; Matsumoto et al., 2002). There have been a number of paleoceanographic studies that directly attempted to test this hypothesis with as yet no conclusive verdict (Matsumoto and Sarmiento, 2008). With key Si^* features captured by MESMO 2, it can be used to further understand the biogeochemical implications of climate-carbon feedbacks involving diatoms.

In this regard, it would be helpful to also simulate $\delta^{30}Si$ in seawater. Because it becomes heavier in a parcel of seawater as $Si(OH)_4$ utilization increases, measurements of $\delta^{30}Si$ in deep sea sediments offer an exciting possibility to investigate past changes in the marine silica cycle. Already a number of studies have made measurements of different sedimentary fractions such as opal (Horn et al., 2011) and sponge spicules (Ellwood et al., 2010).

To date, there are two modeling studies of seawater δ^{30}Si. First, Wischmeyer et al. (2003) used an ocean general circulation model with a prognostic PO_4-based export production, which is then related to Si production. Second, Reynolds (2009) used a box model, in which diagnostic PO_4-based production is again related to Si production. With a more realistic and mechanistic representation of the marine silica cycle, MESMO 2 makes significant improvements over these earlier efforts. As in Wischmeyer et al. (2003), the −1.1 ‰ fractionation during silicic acid uptake imparts a heavy δ^{30}Si signal to surface waters (Fig. 10a) that experience a greater degree of $Si(OH)_4$ utilization (Fig. 10b). The surface map of δ^{30}Si (Figure 10c) resembles the subtropical gyres and POC production (Figs. 6, 7). However, it is more complicated, because surface $Si(OH)_4$ is decoupled from other nutrients though its dependence on Fe and variable Si:N uptake ratio.

4.2 The terrestrial biosphere

The calibration of the ENTS parameters in MESMO 2E produces 123 PgC yr^{-1} for global net photosynthesis, 62 PgC yr^{-1} for vegetation respiration, and 61 PgC yr^{-1} for leaf litter and soil respiration (Table 1). The leaf litter flux represents the influx for soil carbon reservoir and soil respiration represents its outflux, so they are equal at steady state. These fluxes compare well to those presented by IPCC preindustrial estimates of 120 PgC yr^{-1} for photosynthesis and 60 PgC yr^{-1} for the other fluxes (Houghton et al., 2001). The carbon stock in MESMO 2E is 461 PgC in above ground vegetation and 1319 PgC in soils (Table 1). In comparison, Williamson et al. (2006) simulated stocks of 437 and 1317 PgC for vegetation and soil respectively in the original description of ENTS. The data-based targets for these stocks are 451 PgC (Olson et al., 1985) and 1306 PgC (Batjes, 1995), which include postindustrial land use changes. MESMO 2E simulation represents the preindustrial state in the absence of the effects of human land use changes.

GMDD
5, 2999–3033, 2012

The spatial distribution in carbon vegetation compares favorably to observations (Hall et al., 2005): peak carbon storage in tropical rainforests and secondary maximum in boreal forests (Fig. 11a). It also captures the main desert regions of the world. Soil carbon distribution reasonably shows high values in northern boreal regions, where low temperatures limit soil respiration, and low values in the tropical regions, where temperatures and thus soil respiration rate are high (Fig. 11b). In terms of $\Delta^{14}C$, the vegetation is very close to being in equilibrium with the atmosphere (i.e.,~ 0 ‰), as expected. Soil is more depleted especially in cold regions such as Alaska and Siberia where low respiration rates lead to longer residence times of carbon (Fig. 11c).

5 Summary

Two new versions of MESMO are presented here: MESMO 2 and MESMO 2E. The only differences between the two are the coupling of a terrestrial biosphere model ENTS in the latter and the planetary albedo adjustment needed to compensate for the change in land surface albedo caused by the coupling. The physical and biogeochemical modifications described here (Table 2) correct unrealistically low surface albedo values on ice sheets, introduce more seasonality, and allow more explicit representation of the marine silica cycle as compared to MESMO 1.

The use of the same seasonal ECMWF winds to drive all aspects of MESMO 2 removes the inconsistency that existed in the previous version, in which different wind products were used to drive ocean dynamics, air-sea gas exchange, atmospheric heat and moisture transport, and ENTS. Compared to the earlier annual winds, the new seasonal winds impart more momentum to the Southern Ocean in particular, causing the ocean interior to become excessively well ventilated. This necessitated adjustments in the existing wind scaling factor and interbasin freshwater flux in order to realize distributions of natural $\Delta^{14}C$ and anthropogenic transient tracers that are consistent with observations.

GMDD
5, 2999–3033, 2012

The implementations of the existing Fe code, two classes of phytoplankton, and a dependence of the $Si(OH)_4$ utilization on Fe availability are sufficient to simulate key features of the marine silica cycle. They include large $Si(OH)_4$ limitation for diatoms in much of the low latitude oceans, elevated Si:N uptake ration in the Southern Ocean and the far North Pacific, $Si(OH)_4$ depletion in the Southern Ocean, and most importantly the export of $Si(OH)_4$ depletion to the rest of the world ocean via Antarctic Intermediate/Mode Water. These features make MESMO 2 appropriate for future investigation of climate-carbon feedbacks involving diatoms, which have received attention especially in the paleoclimate context.

Supplementary material related to this article is available online at: http://www.geosci-model-dev-discuss.net/5/2999/2012/gmdd-5-2999-2012-supplement.zip.

Acknowledgements. Model development efforts were supported at the University of Minnesota by the McKnight Land Grant Professorship to KM. Efforts by KM elsewhere during sabbatical were supported by visiting fellowships from the University of Tokyo, University of Tasmania, and University of New South Wales. AH and HJW were supported by a summer REU internship program at the University of Minnesota, made possible by grants from the US National Science Foundation (EAR1004258, 1062775).

References

Archer, D., Eby, M., Brovkin, V., Ridgwell, A., Cao, L., Mikolajewicz, U., Caldeira, K., Matsumoto, K., Munhoven, G., Montenegro, A., and Tokos, K.: Atmospheric lifetime of fossil fuel carbon dioxide, Ann. Rev. Earth Planet. Sci., 37, 117–134, 2009.

Archer, D. and Johnson, K.: A model of the iron cycle in the ocean, Glob. Biogeochem. Cy., 14, 269–279, 2000.

GMDD

5, 2999–3033, 2012

MESMO 2: a mechanistic marine silica cycle

K. Matsumoto et al.

Armstrong, R., Lee, C., Hedges, J., Honjo, S., and Wakeham, S. G.: A new, mechanistic model for organic carbon fluxes in the ocean based on the quantitative association of POC with mineral ballasts, Deep Sea Research, Pt. II, 49, 219–236, 2002.

Batjes, N. H.: A homogenized soil data file for global environmental research: A subset of FAO, ISRIC and NRCS profiles (Version 1.0), International Soil Reference and Information Centre, Wageningen, The Netherlands, 1995.

Boyd, P. and Ellwood, M. J.: The biogeochemical cycle of iron in the ocean, Nat. Geosci., 3, 10, doi:10.1038/ngeo0964, 2010.

Brzezinski, M. A., Pride, C. J., Sigman, D. M., Sarmiento, J. L., Matsumoto, K., Gruber, N., Rau, G. H., and Coale, K. H.: A switch from $Si(OH)_4$ to NO_3^- depletion in the glacial Southern Ocean, Geophys. Res. Lett., 29, doi:10.1029/2001GL014349, 2002.

Cao, L., Eby, M., Ridgwell, A., Caldeira, K., Archer, D., Ishida, A., Joos, F., Matsumoto, K., Mikolajewicz, U., Mouchet, A., Orr, J. C., Plattner, G.-K., Schlitzer, R., Tokos, K., Totterdell, I., Tschumi, T., Yamanaka, Y., and Yool, A.: The role of ocean transport in the uptake of anthropogenic CO_2, Biogeosciences, 6, 375–390, doi:10.5194/bg-6-375-2009, 2009.

Claussen, M., Mysak, L. A., Weaver, A., Crucifix, M., Fichefet, T., Loutre, M. F., Weber, S. L., Alcamo, J., Alexeev, V., A., Berger, A., Calov, R., Ganopolski, A., Goosse, H., Lohmann, G., Lunkeit, F., Mokhov, I. I., Petoukhov, V., Stone, P., and Wang, Z.: Earth system models of intermediate complexity: Closing the gap in the spectrum of climate system models, Clim. Dynam., 18, 579–586, 2002.

De La Rocha, C. L., Brzezinksi, M. A., and DeNiro, M. J.: Fractionation of silicon isotopes by marine diatoms during biogenic silica formation, Geochim. Cosmochemica Acta, 61, 5051–5056, 1997.

De La Rocha, C. L., Brzezinski, M. A., DeNiro, M. J., and Shemesh, A.: Silicon-isotope composition of diatoms as an indicator of past oceanic change, Nature, 395, 680–683, 1998.

Dunne, J., Sarmiento, J., and Gnanadesikan, A.: A synthesis of global particle export from the surface ocean and cycling through the ocean interior and on the seafloor, Glob. Biogeochem. Cy., 21, GB4006, doi:10.1029/2006GB002907, 2007.

Eby, M., Weaver, A. J., Alexander, K., Zickfeld, K., Abe-Ouchi, A., Cimatoribus, A. A., Crespin, E., Drijfhout, S. S., Edwards, N. R., Eliseev, A. V., Feulner, G., Fichefet, T., Forest, C. E., Goosse, H., Holden, P. B., Joos, F., Kawamiya, M., Kicklighter, D., Kienert, H., Matsumoto, K., Mokhov, I. I., Monier, E., Olsen, S. M., Pedersen, J. O. P., Perrette, M., Philippon-Berthier, G., Ridgwell, A., Schlosser, A., Deimling, T. S. v., Shaffer, G., Smith, R. S., Spahni, R., Sokolov,

GMDD

5, 2999–3033, 2012

MESMO 2: a mechanistic marine silica cycle

K. Matsumoto et al.

A. P., Steinacher, M., Tachiiri, K., Tokos, K., Yoshimori, M., Zeng, N., and Zhao, F.: Historical and idealized climate model experiments: An EMIC intercomparison, Clim. Past, accepted, 2012.
Edwards, N. R. and Marsh, R.: Uncertainties due to transport-parameter sensitivity in an efficient 3-D ocean-climate model, Climate Dynam., 24, 415–433, 2005.
Ellwood, M. J., Wille, M., and Maher, W.: Glacial silicic acid concentrations in the Southern Ocean, Science, 330, 1088–1091, 2010.
Foster, T. D. and Carmack, E. C.: Frontal zone mixing and Antarctic bottom water formation in the southern Weddell Sea, Deep-Sea Res., 23, 301–317, 1976.
Franck, V. M., Brzezinski, M. A., Coale, K. H., and Nelson, D. M.: Iron and silicic acid concentrations regulate Si uptake north and south of the Polar Frontal Zone in the Pacific sector of the Southern Ocean, Deep Sea Res. Pt. II, 47, 3315–3338, 2000.
Hall, F. G., Collatz, G. J., Los, S. O., de Colstoun, E. B., and Landis, D.: ISLSCP Initiative II, NASA, 2005.
Horn, M. G., Beucher, C. P., Robinson, R. S., and Brzezinski, M. A.: Southern ocean nitrogen and silicon dynamics during the last deglaciation, Earth Planet. Sci. Lett., 310, 334–339, 2011.
Houghton, J. T., Ding, Y., Griggs, D. J., Noguer, M., van der Linden, P. J., and Xiaosu, D.: Climate Change 2001 - The Scientific Basis: Contribution of Working Group I to the Third Assessment Report of the Intergovernmental Panel on Climate Change. Cambridge University Press, Cambridge, 944 pp., 2001.
Hutchins, D. A. and Bruland, K. W.: Iron-limited diatom growth and Si:N uptake ratios in coastal upwelling regime, Nature, 393, 561–564, 1998.
Johnson, K. S., Gordon, R. M., and Coale, K. H.: What controls dissolved iron concentrations in the world ocean?, Mar. Chem., 57, 137–161, 1997.
Jones, P. D., New, M., Parker, D. E., Martin, S., and Rigor, I. G.: Surface air temperature and its changes over the past 150 years, Rev. Geophys., 37, 173–199, 1999.
Joos, F., Roth, R., Fuglestvedt, J. S., Peters, G. P., Enting, I. G., Bloh, W. v., Brovkin, V., Burke, E. J., Eby, M., Edwards, N. R., Friedrich, T., Frolicher, T. L., Halloran, P. R., Holden, P. B., Jones, C., Kleinen, T., Mackenzie, F., Matsumoto, K., Meinshausen, M., Plattner, G.-K., Reisinger, A., Segschneider, J., Shaffer, G., Steinacher, M., Strassmann, K., Tanaka, K., Timmermann, A., and Weaver, A. J.: Carbon dioxide and climate impulse response functions

GMDD
5, 2999–3033, 2012

MESMO 2: a mechanistic marine silica cycle

K. Matsumoto et al.

for the computation of greenhouse gas metrics: A multi-model model analysis, Atmos. Chem. Phys., in review, 2012.

Josey, S. A., Kent, C., and Taylor, P. K.: Wind stress forcing of the ocean in the SOC Climatology: Comparisons with the NCEP-NCAR, ECMWF, UWM/COADS, and Hellerman and Rosenstein datasets, J. Phys. Oceanogr., 32, 1993–2019, 2002.

Josey, S. A., Kent, E. C., and Taylor, P. K.: Report 6: The Southampton Oceanography Centre (SOC) ocean-atmosphere heat, momentum and freshwater flux atlas, Southampton Oceanography Centre, Southampton, 1998.

Kalnay, E., Kanamitsu, M., Kistler, R., Collins, W., Deaven, D., Gandin, L., Iredell, M., Saha, S., White, G., Woollen, J., Zhu, Y., Chelliah, M., Ebisuzaki, W., Higgins, W., Janowiak, J., Mo, K. C., Ropelewski, C., Wang, J., Leetmaa, A., Reynolds, R., Jenne, R. and Joseph, D.: The NCEP/NCAR 40-year reanalysis project, Bull. Am. Meterol. Soc., 77, 437–471, 1996.

Key, R., Kozyr, A., Sabine, C., Lee, K., Wannikhof, R., Bullister, J. L., Feeley, R. A., Millero, F., Mordy, C., and Peng, T.-H.: A global ocean carbon climatology: Results from GLODAP, Global Biogeochem. Cy., 18, GB4031, doi:10.1029/2004GB002247, 2004.

Lee, S., Chiang, J., Matsumoto, K., and Tokos, K.: Southern Ocean wind response to North Atlantic cooling and the rise in atmospheric CO_2: Modeling perspective and paleoceanographic implications, Paleoceanography, 26, PA1214, doi:10.1029/2010PA002004, 2011.

Levitus, S. and Boyer, T. P.: World ocean atlas 1994, Volume 4: Temperature, National Oceanic and Atmospheric Administration, Washington, 1994.

Levitus, S., Burgett, R. and Boyer, T. P.: World ocean atlas 1994, Volume 3: Salinity, National Oceanic and Atmospheric Administration, Washington, 1994.

Levitus, S., Conkright, M. E., Reid, J. L., Najjar, R. G., and Mantyla, A.: Distribution of nitrate, phosphate and silicate in the world oceans, Progr. Oceanogr., 31, 245–273, 1993.

Mahowald, N., Luo, C., del Corral, J., and Zender, C. S.: Interannual variability in atmospheric mineral aerosols from a 22-year model simulation and observational data, J. Geophys. Res., 108, 4352, doi:10.1029/2002JD002821, 2003.

Matsumoto, K. and Sarmiento, J. L.: A corollary to the silicic acid leakage hypothesis, Paleoceanography, 23, PA2203, doi:10.1029/2007PA001515, 2008.

Matsumoto, K., Sarmiento, J. L., and Brzezinski, M. A.: Silicic acid leakage from the Southern Ocean: A possible explanation for glacial atmospheric pCO_2, Global Biogeochem. Cy., 16, doi:10.1029/2001GB001442, 2002.

Matsumoto, K., Sarmiento, J. L., Key, R. M., Aumont, O., Bullister, J. L., Caldeira, K., Campin, J.-M., Doney, S. C., Drange, H., Dutay, J.-C., Follows, M., Gao, Y., Gnanadesikan, A., Gruber, N., Ishida, A., Joos, F., Lindsay, K., Maier-Reimer, E., Marshall, J. C., Matear, R. J., Monfray, P., Mouchet, A., Najjar, R., Plattner, G.-K., Schlitzer, R., Slater, R., Swathi, P. S., Totterdell, I. J., Weirig, M.-F., Yamanaka, Y., Yool, A., and Orr, J. C.: Evaluation of ocean carbon cycle models with data-based metrics, Geophys. Res. Lett., 31, L07303, doi:10.1029/2003GL018970, 2004.

Matsumoto, K., Tokos, K., Chikamoto, M. O., and Ridgwell, A.: Characterizing postindustrial changes in the natural ocean carbon cycle in an Earth system model, Tellus, 62B, 296–313, 2010.

Matsumoto, K., Tokos, K. S., Price, A. R., and Cox, S. J.: First description of the Minnesota Earth System Model for Ocean biogeochemistry (MESMO 1.0), Geosci. Model Dev., 1, 1–15, doi:10.5194/gmd-1-1-2008, 2008.

Olson, J. S., Watts, J. A., and Allison, L. J.: Major world ecosystem complexes ranked by carbon in live vegetation. NDP-017, Carbon Dioxide Information Analysis, Oak Ridge National Laboratory, Oak Ridge, Tenessee, 1985.

Olson, J. S., Watts, V. A., and Allison, L. J.: Carbon in live vegetation of major world ecosystems. ORNL-5862, Oak Ridge National Lab., Oak Ridge, Tenn., 1983.

Parekh, P., Follows, M., and Boyle, E.: Decoupling of iron and phosphate in the global ocean, Glob. Biogeochem. Cy., 19, GB2020, doi:10.1029/2004GB002280, 2005.

Reynolds, B. C.: Modeling the modern marine δ^{30}Si distribution, Glob. Biogeochem. Cy., 23, GB2015, doi:10.1029/2008GB003266, 2009.

Ridgwell, A. J., Watson, A. J., and Archer, D. E.: Modeling the response of the oceanic Si inventory to perturbation, and consequences for atmospheric CO2, Glob. Biogeochem. Cy., 16, 4, doi:10.1029/2002GB001877, 2002.

Sabine, C. L., Feeley, R. A., Gruber, N., Key, R. M., Lee, K., Bullister, J. L., Wanninkhof, R., Wong, C. S., Wallace, D. W. R., Tilbrook, B., Millero, F. J., Peng, T.-H., Kozyr, A., Ono, T., and Rios, A. F.: The oceanic sink for anthropogenic CO_2, Science, 305, 367–371, 2004.

Sarmiento, J. L. and Gruber, N.: Ocean Biogeochemical Dynamics, Princeton University Press, Princeton, 503 pp., 2006.

Sarmiento, J. L., Gruber, N., Brzezinski, M. A., and Dunne, J. P.: High-latitude controls of thermocline nutrients and low latitude biological productivity, Nature, 427, 56–60, 2004.

GMDD
5, 2999–3033, 2012

MESMO 2: a mechanistic marine silica cycle

K. Matsumoto et al.

Sun, X. and Matsumoto, K.: Effects of sea ice on atmospheric pCO_2: A revised view and implications for glacial and future climates, J. Geophys. Res., 115, G02015, doi:10.1029/2009JG001023, 2010.
Sunda, W. G. and Huntsman, S. A.: Iron uptake and growth limitation in oceanic and coastal phytoplankton, Mar. Chem., 50, 189–206, 1995.
Takeda, S.: Influence of iron availability of nutrient consumption ratio of diatoms in oceanic waters, Nature, 393, 774–777, 1998.
Trenberth, K. E., Olson, J., and Large, W.: A global ocean wind stress climatology based on ECMWF analyses. Tech. Rep. NCAR/TN-338+STR, National Center for Atmospheric Research, Boulder, 1989.
Ushie, H. and Matsumoto, K.: The role of shelf nutrients on glacial-interglacial CO_2: A negative feedback, Glob. Biogeochem. Cy., 26, GB2039, doi:10.1029/2011GB004147, 2012.
Weaver, A., Sedlacek, J., Eby, M., Alexander, K., Crespin, E., Fichefet, T., Philippon-Berthier, G., Joos, F., Kawamiya, M., Matsumoto, K., Steinacher, M., Tachiiri, K., Tokos, K., Yoshimori, M., and Zickfeld, K.: Stability of the Atlantic meridional overturning circulation: A model intercomparison, Geophys. Res. Lett., submitted, 2012.
Willey, D. A., Fine, R. A., Sonnerup, R., Bullister, J. L., Smethie, M. W., and Warner, M. J.: Global oceanic chlorofluorocarbon inventory, Geophys. Res. Lett., 31, L01303, doi:10.1029/2003GL018816, 2004.
Williamson, M. S., Lenton, T. M., Shepherd, J. G., and Edwards, N. R.: An efficient numerical terrestrial scheme (ENTS) for Earth system modeling, Ecol. Model., 198, 362–374, 2006.
Wischmeyer, A. G., De La Rocha, C. L., Maier-Rainer, E., and Wolf-Gladrow, D.: Control mechanisms for oceanic distribution of silicon isotopes, Glob. Biogeochem. Cy., 17, doi:10.1029/2002GB002022, 2003.
Zickfeld, K., Eby, M., Alexander, K., Weaver, A. J., Crespin, E., Fichefet, T., Goosse, H., Philippon-Berthier, G., Edwards, N. R., Holden, P. B., Eliseev, A. V., Mokhov, I., Feulner, G., Kienert, H., Perrette, M., Forest, C. E., Friedlingstein, P., Joos, F., Spahni, R., Steinacher, M., Kawamiya, M., Tachiiri, K., Kicklighter, D., Monier, E., Schlosser, A., Sokolov, A., Matsumoto, K., Tokos, K. S., Olsen, S. M., Pedersen, J. O. P., Ridgwell, A., Shaffer, G., Yoshimori, M., Zeng, N., and Zhao, F.: Long-term climate change commitment and reversibility: An EMIC intercomparison, J. Climate, submitted, 2012.

GMDD
5, 2999–3033, 2012

MESMO 2: a mechanistic marine silica cycle

K. Matsumoto et al.

Table 1. Equilibrium model states.

	Unit	Constraints	MESMO 1	MESMO 2	MESMO 2E
Simulation ID#			090309a 090415b	120531a/m/n	120531b/x/y
Global physical					
Mean surf air temp	°C	14.0	11.4	13.5	13.6
Mean SST	°C	18.5	17.6	18.5	17.4
Mean SSS	PSU	34.6	34.7	34.7	34.4
Atlantic MOC	$10^6\ m^3\ s^{-1}$	14–27	12	12	17
Arctic sea ice, Feb	$10^6\ km^2$	14–16	21	20	18
Antarctic sea ice, Sept	$10^6\ km^2$	17–20	34	33	26
NADW $\Delta^{14}C$	‰	-67 ± 29	−99	−104	−92
CDW $\Delta^{14}C$	‰	-155 ± 12	−153	−156	−145
NPDW $\Delta^{14}C$	‰	-226 ± 14	−216	−196	−190
Ocean carbon					
POC production	Pg-C y^{-1}	9.6 ± 3.6	10.6	11.9	12.5
Opal production	Tmol-Si y^{-1}	101 ± 35	–	130	139
$CaCO_3$ production	Pg-C y^{-1}	< 1	0.9	1.0	0.9
Terrestrial carbon					
Net photosynthesis	Pg-C y^{-1}	120	–	–	123
Vegetation respiration	Pg-C y^{-1}	60	–	–	62
Leaf litter/soil respiration	Pg-C y^{-1}	60	–	–	61
Land Veg. Carbon	Pg-C	451	–	–	462
Soil Carbon	Pg-C	1306	–	–	1319
1994 tracer inventories					
CFC-11	10^6 mole	0.55 ± 0.12	0.69	0.56	0.59
Anthropogenic carbon	Pg-C	118 ± 19	118	100	101

Mean SST and SSS based on 1994 World Ocean Atlas (Levitus and Boyer, 1994, Levitus et al., 1994). For other constraints, see the main text for their sources.

GMDD
5, 2999–3033, 2012

Table 2. Model parameters.

	Unit	MESMO 1	MESMO 2	MESMO 2E
Physical model				
Ice sheet albedo		0.5	0.8	0.8
Change in planetary albedo		0 %	−3.5 %	−5.5 %
Wind stress		Annual NCEP	Seasonal ECMWF	Seasonal ECMWF
Wind scaling		2.0 globally	2.0 in N. Atlantic	2.0 in N. Atlantic
FW flux adjustment in north	$10^6\,m^3\,s^{-1}$	0.2	0.3	0.3
FW flux adjustment in south	$10^6\,m^3\,s^{-1}$	−0.03	−0.13	−0.13
Biogeochemical model				
LP: Optimal nutrient uptake	Yr^{-1}		0.01	0.01
SM: Optimal nutrient uptake	Yr^{-1}		0.16	0.16
LP: K_{PO4}	$\mu mol\,kg^{-1}$		0.39	0.39
SM: K_{PO4}	$\mu mol\,kg^{-1}$		0.03	0.03
LP: K_{NO3}	$\mu mol\,kg^{-1}$		5.00	5.00
SM: K_{NO3}	$\mu mol\,kg^{-1}$		0.50	0.50
LP: K_{CO2}	$\mu mol\,kg^{-1}$		0.925	0.925
SM: K_{CO2}	$\mu mol\,kg^{-1}$		0.075	0.075
LP: K_{Fe}	$nmol\,kg^{-1}$		0.10	0.10
SM: K_{Fe}	$nmol\,kg^{-1}$		0.01	0.01
$K_{Si(OH)4}$	$\mu mol\,kg^{-1}$		1.00	1.00
Cond. Stability, ligand-bound Fe			1.25×10^{11}	1.25×10^{11}
Fe scavenging rate by POC			0.7	0.7
Particle sinking speed		$50\,m\,d^{-1}$	$30\,m\,d^{-1}$	$30\,m\,d^{-1}$
Maximum Fe:C			200 000	200 000
Terrestrial scheme ENTS				
k18 (photosynthesis)		–	–	2.392
k24 (vegetation respiration)		–	–	0.172
k29 (soil respiration)		–	–	0.0725

LP = large phytoplankton; SM = Small phytoplankton.

Discussion Paper | Discussion Paper | Discussion Paper | Discussion Paper |

GMDD

5, 2999–3033, 2012

MESMO 2: a mechanistic marine silica cycle

K. Matsumoto et al.

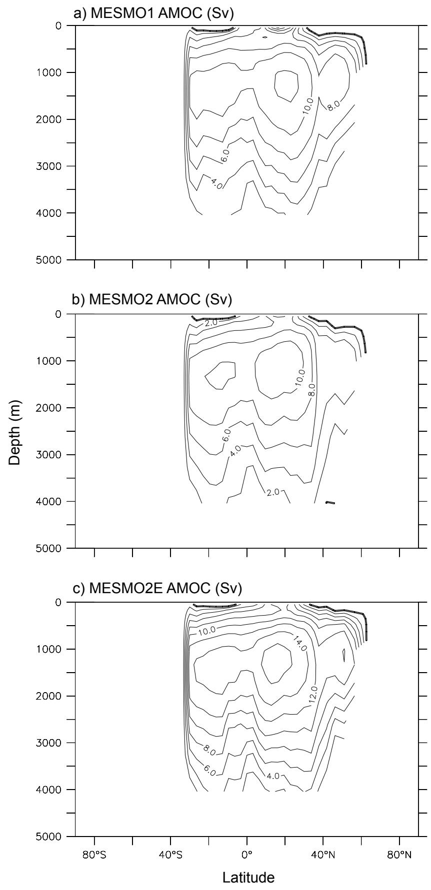

Fig. 1. The Atlantic meridional overturning circulation in three versions of MEMSO.

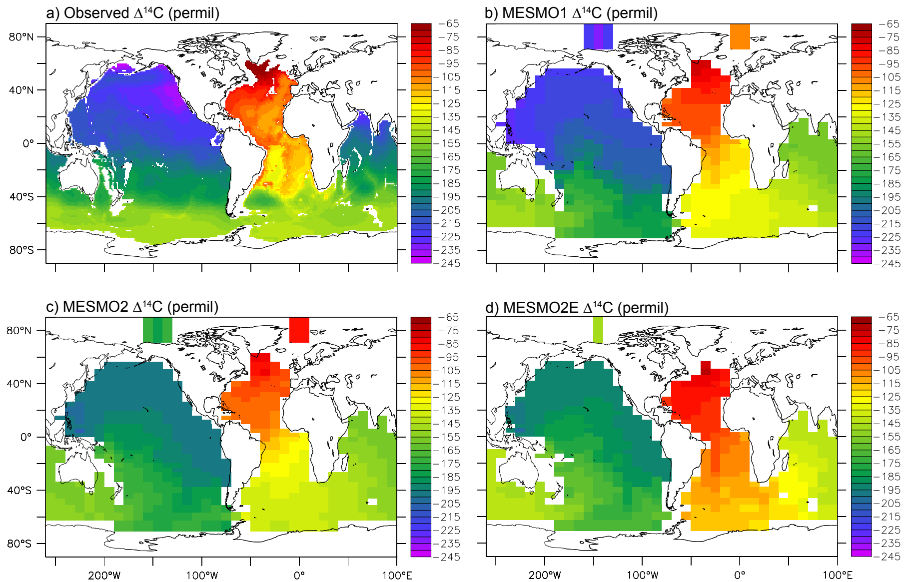

Fig. 2. Observed and model-simulated natural $\Delta^{14}C$ from 2500–5000 m water depth. Observations are based on WOCE data (Key et al., 2004).

GMDD
5, 2999–3033, 2012

MESMO 2: a mechanistic marine silica cycle

K. Matsumoto et al.

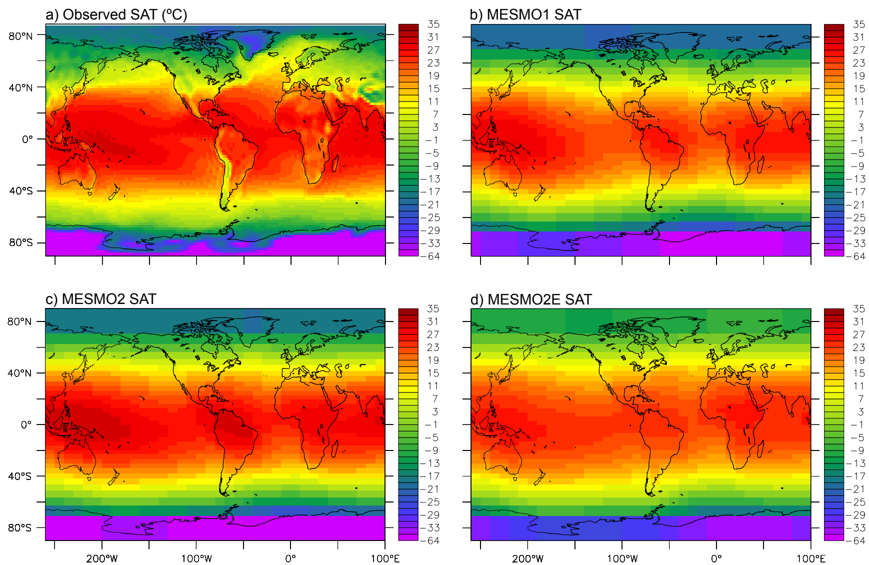

Fig. 3. Observed and model-simulated annual mean surface air temperature. Observations are based on the NCEP/NCAR 40 yr reanalysis (Kalnay et al., 1996).

GMDD
5, 2999–3033, 2012

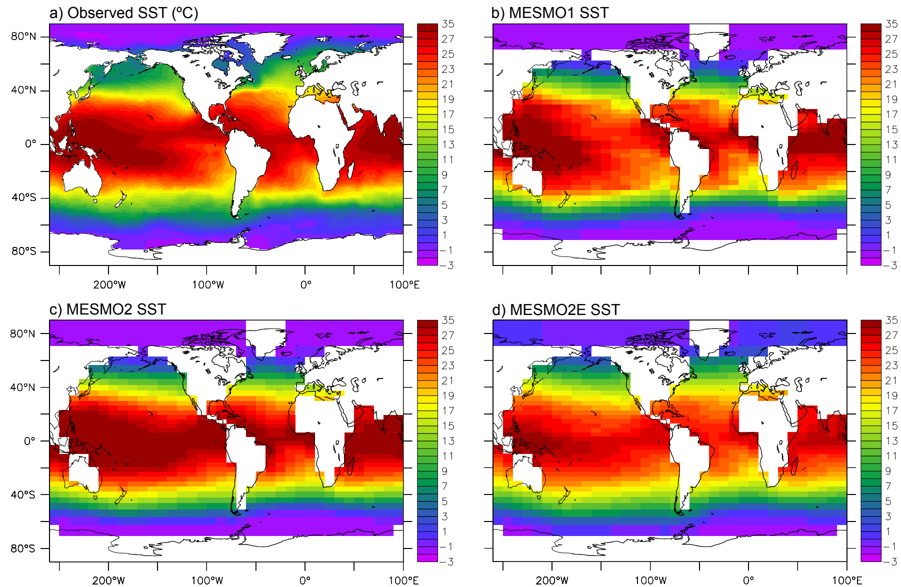

Fig. 4. Observed and model-simulated sea surface temperature. Observations are based on Levitus et al. (1994).

GMDD

5, 2999–3033, 2012

MESMO 2: a mechanistic marine silica cycle

K. Matsumoto et al.

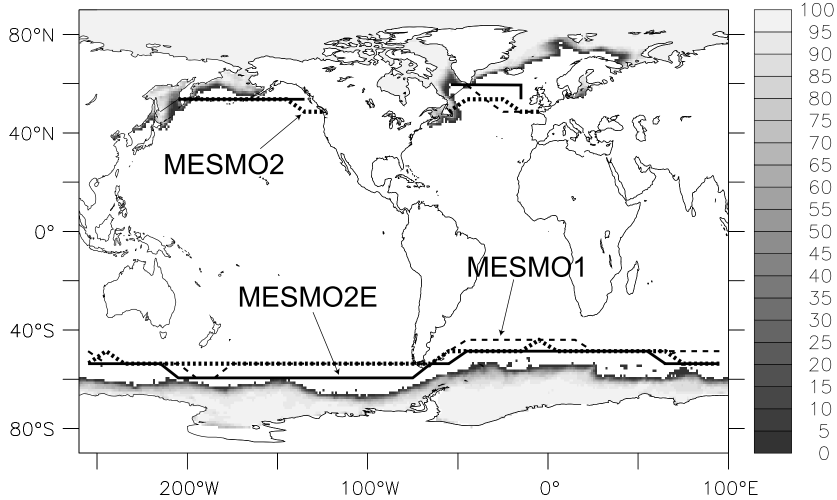

Fig. 5. Observed and model-simulated maximum seasonal sea ice extent. Observations indicated in greyscale are based on satellite-based passive microwave data (1/1987–12/1988) archived at the National Snow and Ice Data Center (A. Nomura and R. Grumbine, personal communication, 1995).

GMDD
5, 2999–3033, 2012

MESMO 2: a mechanistic marine silica cycle

K. Matsumoto et al.

Title Page
Abstract | Introduction
Conclusions | References
Tables | Figures
◀| |▶
◀ ▶
Back | Close
Full Screen / Esc
Printer-friendly Version
Interactive Discussion

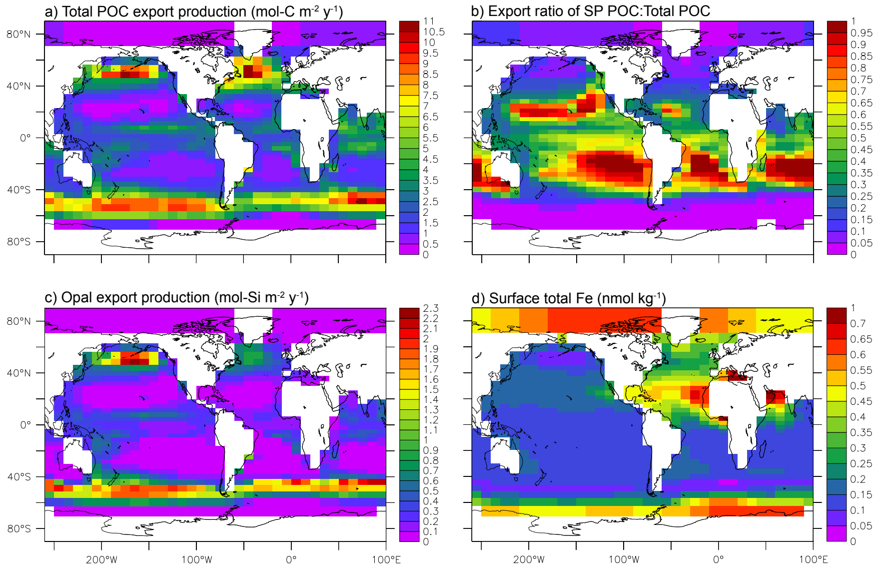

Fig. 6. Simulated annual mean results from MESMO 2: **(a)** export carbon production; **(b)** fractional contribution of the small phytoplankton to the total export carbon production; **(c)** export opal production; **(d)** surface total Fe (FeL+free Fe) concentration.

GMDD
5, 2999–3033, 2012

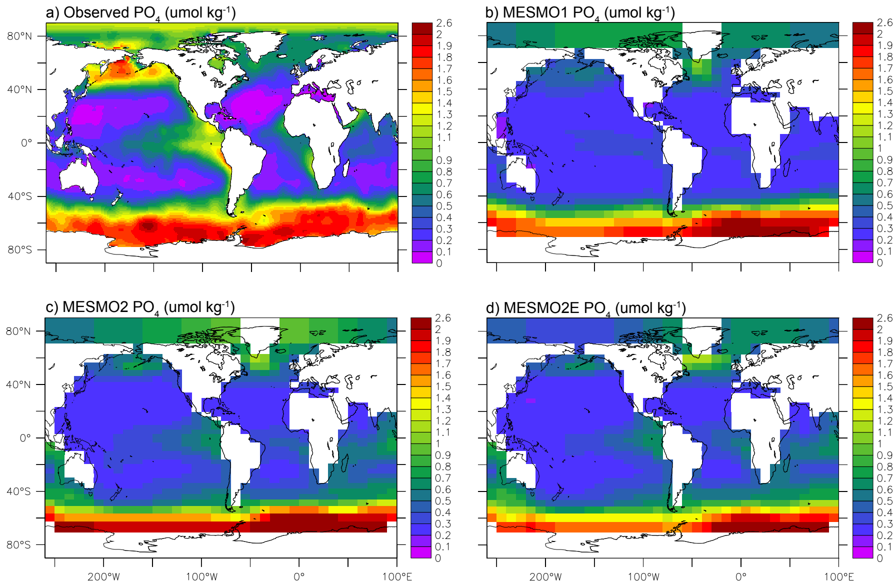

Fig. 7. Observed and model-simulated annual mean PO4 concentration in the top 100 m. Observations are based on Levitus et al. (1993).

GMDD
5, 2999–3033, 2012

MESMO 2: a mechanistic marine silica cycle

K. Matsumoto et al.

Title Page
Abstract
Introduction
Conclusions
References
Tables
Figures
◀
▶
Back
Close
Full Screen / Esc
Printer-friendly Version
Interactive Discussion

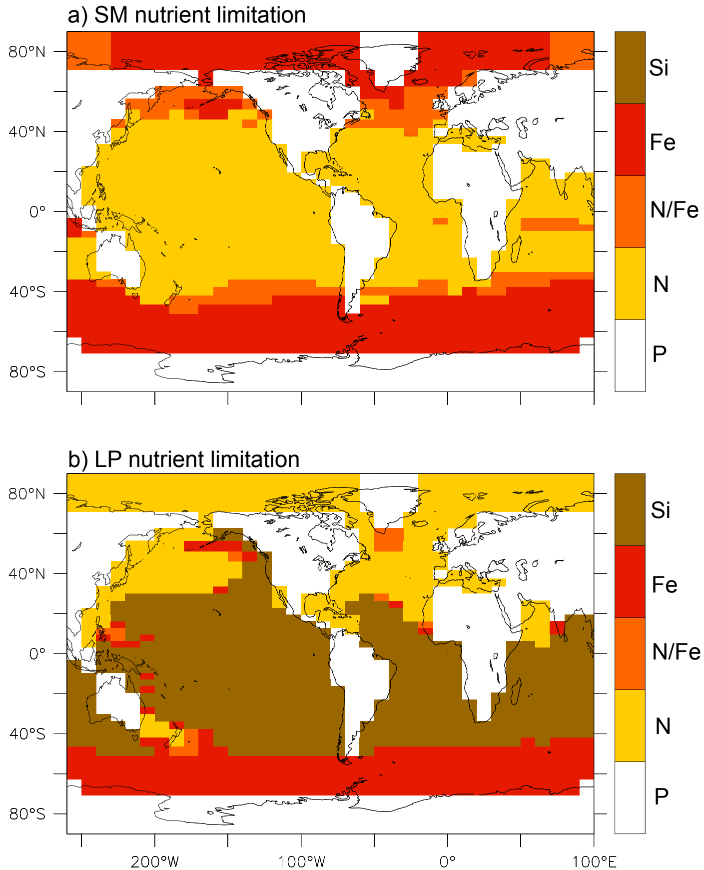

Fig. 8. Simulated annual mean nutrient limitations for the small phytoplankton **(a)** and large phytoplankton **(b)** from MESMO 2.

GMDD
5, 2999–3033, 2012

MESMO 2: a mechanistic marine silica cycle

K. Matsumoto et al.

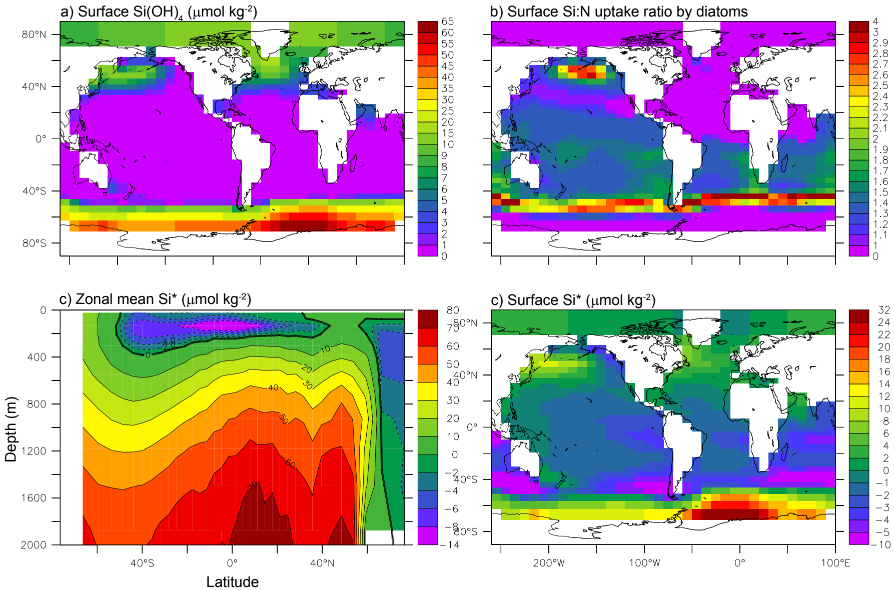

Fig. 9. Simulated annual mean results from MESMO 2: **(a)** surface silicic acid concentration; **(b)** uptake ratio of silicic acid to nitrate by diatoms in the surface waters; **(c)** zonally averaged Si* concentration; **(d)** surface Si* concentration. Negative Si* indicates Si deficiency; see text.

GMDD
5, 2999–3033, 2012

MESMO 2: a mechanistic marine silica cycle

K. Matsumoto et al.

Title Page
Abstract | Introduction
Conclusions | References
Tables | Figures
◀| |▶
◀ ▶
Back | Close
Full Screen / Esc
Printer-friendly Version
Interactive Discussion

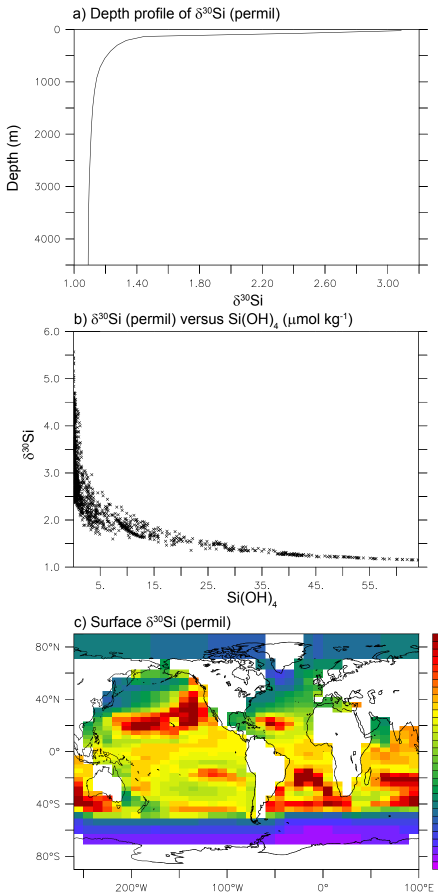

Fig. 10. Simulated annual mean δ^{30}Si from MESMO 2: **(a)** vertical profile; **(b)** relationship to silicic acid; and **(c)** surface distribution.

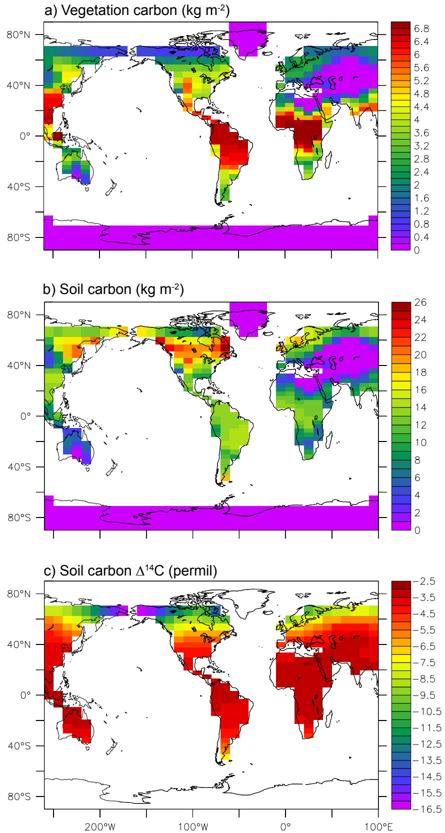

Fig. 11. Simulated annual mean terrestrial biosphere results from MESMO 2E: **(a)** vegetation carbon stock; **(b)** soil carbon stock; and **(c)** soil Δ^{14}C.

GMDD
5, 2999–3033, 2012

MESMO 2: a mechanistic marine silica cycle

K. Matsumoto et al.

Title Page
Abstract | Introduction
Conclusions | References
Tables | Figures
◀| |▶
◀ ▶
Back | Close
Full Screen / Esc
Printer-friendly Version
Interactive Discussion